Catalysis Science & Technology

PAPER

View Article Online
View Journal | View Issue

Cite this: *Catal. Sci. Technol.*, 2017, 7, 1167

Nanograined surface shell wall controlled ZnO–ZnS core–shell nanofibers and their shell wall thickness dependent visible photocatalytic properties†

Kuglaur Shanmugam Ranjith,*[a] Anitha Senthamizhan,[a] Brabu Balusamy[a] and Tamer Uyar*[ab]

The core–shell form of ZnO–ZnS based heterostructural nanofibers (NF) has received increased attention for use as a photocatalyst owing to its potential for outstanding performance under visible irradiation. One viable strategy to realize the efficient separation of photoinduced charge carriers in order to improve catalytic efficiency is to design core–shell nanostructures. But the shell wall thickness plays a vital role in effective carrier separation and lowering the recombination rate. A one dimensional (1D) form of shell wall controlled ZnO–ZnS core–shell nanofibers has been successfully prepared *via* electrospinning followed by a sulfidation process. The ZnS shell wall thickness can be adjusted from 5 to 50 nm with a variation in the sulfidation reaction time between 30 min and 540 min. The results indicate that the surfaces of the ZnO nanofibers were converted to a ZnS shell layer *via* the sulfidation process, inducing visible absorption behavior. Photoluminescence (PL) spectral analysis indicated that the introduction of a ZnS shell layer improved electron and hole separation efficiency. A strong correlation between effective charge separation and the shell wall thickness aids the catalytic behavior of the nanofiber network and improves its visible responsive nature. The comparative degradation efficiency toward methylene blue (MB) has been studied and the results showed that the ZnO–ZnS nanofibers with a shell wall thickness of ~20 nm have 9 times higher efficiency than pristine ZnO nanofibers, which was attributed to effective charge separation and the visible response of the heterostructural nanofibers. In addition, they have been shown to have a strong effect on the degradation of Rhodamine B (Rh B) and 4-nitrophenol (4-NP), with promising reusable catalytic efficiency. The shell layer upgraded the nanofiber by acting as a protective layer, thus avoiding the photocorrosion of ZnO during the catalytic process. A credible mechanism for the charge transfer process and a mechanism for photocatalysis supported by trapping experiments in the ZnO–ZnS heterostructural system for the degradation of an aqueous solution of MB are also explicated. Trapping experiments indicate that h^+ and $^{\bullet}OH$ are the main active species in the ZnO–ZnS heterostructural catalyst, which do not effectively contribute in a bare ZnO catalytic system. Our work also highlights the stability and recyclability of the core–shell nanostructure photocatalyst and supports its potential for environmental applications. We thus anticipate that our results show broad potential in the photocatalysis domain for the design of a visible light functional and reusable core–shell nanostructured photocatalyst.

Received 7th December 2016,
Accepted 31st January 2017

DOI: 10.1039/c6cy02556k

rsc.li/catalysis

Introduction

In recent years, the one dimensional (1D) fiber forms of nanomaterials such as metal oxide nanofibers (NF) and their hybrid structural forms have been explored worldwide as functional elements for potential applications, with fundamental scientific interest in their use in chemical and gas sensors,[1] filtration,[2] catalysts,[3] photo electrochemical cells,[4] electrodes for supercapacitors[5] and biomolecular devices.[6] Especially, 1D forms of heterostructures have received promising attention due to their hybrid functional properties, which can give

[a] *UNAM – National Nanotechnology Research Center, Bilkent University, Ankara, 06800, Turkey. E-mail: ranjith@unam.bilkent.edu.tr, uyar@unam.bilkent.edu.tr*
[b] *Institute of Materials Science & Nanotechnology, Bilkent University, Ankara, 06800, Turkey*

† Electronic supplementary information (ESI) available: SEM images of as-prepared electrospun PVA/zinc acetate composites nanofibers, UV-vis absorption spectra, dye degradation spectra with respect to time, and SEM and XPS spectra after catalytic recycling measurements of ZnO and ZnO–ZnS core–shell NFs. See DOI: 10.1039/c6cy02556k

more adaptable functionalities, compared with monolithic nanomaterials, when used in nanoscale devices.[7,8] The core–shell forms of heterostructures are expected to be used widely in the areas of catalysis, and chemical and bio-sensors because of their effective dual functionalities. Extensive interest in heterostructures emerges from their unique electrical, catalytic and electrochemical functionalities, which are closely tied to their high surface-to-volume ratios and, in some instances, exceptional transport properties coupled with confinement effects, 1D transport phenomena, or transport in fractal dimensions.[9] Accordingly, different approaches have evolved to improve the functionalities of hierarchical structures with a wide variety of core–shell nanostructure based building blocks. With their wide band gap natures, metal oxides such as TiO_2 and ZnO are promising photocatalysts in the monolithic phase, and are more efficient in the form of core–shell structures, which improves their functionalities.[4,10,11] Photocatalytic oxidation using these semiconductor materials offers an effective solution, as it allows the complete mineralization of organic dyes into harmless products at a relatively low cost.[12] But, compared to TiO_2, ZnO photocatalysts have some disadvantages, such as their limited photocatalytic efficiency, the easy recombination of electron–hole pairs and their proneness to photocorrosion, which limit their further application. In order to overcome these drawbacks, various ZnO-based nanocomposites with different morphologies have been investigated, to improve the physical and chemical properties.[13,14] Moreover, because of its wide optical and electrical functionality, ZnO is considered an ideal system for the construction of hierarchical structures for catalytic applications. It exhibits vast functionality with a wide bandgap (~3.3 eV), which renders it active exclusively under UV light. Since UV light accounts for only a small fraction of the natural sunlight (~5%) reaching the surface of the earth, shifting the optical response from the UV to the visible range will result in profound benefits for the visible photocatalytic applications of this material. Doping with non-metal elements is an attractive route to alter the electronic properties of ZnO nanostructures, in order to narrow the band gap of wide band gap semiconductors.[15] But improving the charge separation efficiency and avoiding carrier recombination, along with improving visible absorption through constructing a core–shell interface, will effectively improve the photocatalytic activity under visible light.[16,17] Photocatalytic applications involve the interface between the semiconductor surface and adsorbed pollutant molecules. Influence over the interactions between the photocatalyst and pollutant are constrained by the attainable surface. Having control over morphology using templating processes is noteworthy for affecting material performance. But, careful selection of the templating method is a crucial step in perfecting the 1D morphology. One of the widely used fabrication processes for forming 1D NF templates is electrospinning, which is a highly reproducible technique using polymer solutions or melts.[18] Despite intensive research activity over the past few years, the development of innovative fabrication methods providing versatile materials with structural and dimensional flexibility is limited. Inorganic semiconductors (such as PbS,[19] CdS,[10] CdSe,[20] Cu_2S,[17] Ce_2S_3,[21] and Ag_2S (ref. 22)) offer many advantages, such as high extinction coefficients and the capability for optical absorption tailoring over a wider wavelength range. Focusing considerable efforts on designing core–shell architectures with controlled distinctive structural features such as an inner core and outer shell will ameliorate structural functionality. In order to improve the visible photocatalytic behavior, the construction of a typical type II band gap alignment proves highly beneficial, based on previous theoretical and experimental investigations.[23,24]

ZnO–ZnS based core–shell heterostructures specifically exhibit better visible absorption with enhanced catalytic activity with the functionality of a typical type II band gap alignment with minimized lattice mismatch.[24,25] Combining these two wide band gap nanomaterials in the form of a type-II heterostructure can provide an efficient heterostructural semiconductor device design in which the heterostructure band arrangement induces the migration of holes from ZnO to ZnS and electrons from ZnS to ZnO. Decorating a thin layer of ZnS over the ZnO will reduce the surface states and induce charge carrier confinement *via* the type-II band structure.[26] In previous investigations, constructed ZnO–ZnS core–shell nanowire arrays exhibited a pronounced improvement in photoluminescence and photoconductivity as opposed to ZnO nanowire arrays.[26–28] Constructing the shell layer over ZnO or forming semiconductor/ZnO heterojunctions suppressed the recombination of the photoexcited electron–hole pairs of ZnO, which effectively enhances the catalytic activity.[17,28] As it has relatively low toxicity, ZnS has been used to reduce heavy metal toxicity, preventing the formation of Cd^{2+} on the surface of CdSe, and in the detection of Cu^{2+} ions on the ZnO–ZnS surface and the degradation of water pollutants.[29,30] It induces a fast photoresponse time, prevents the influence of oxygen molecules on ZnO conductivity, contributes to high stability in a biological environment and acts as a protective shield to help avoid photocorrosion. A quasi-one-dimensional architecture, a polycrystalline structure and a high surface-to-volume ratio are crucial elements for realizing further applications for electrospun NF in electronic nanodevices. Alternatively to conventional methods for the decoration of a shell layer, the sulfidation process is based on an ion-by-ion growth mechanism that enables the growth of a conformal layer without destroying the original morphology, which can decrease defects in the products and enhance the light-harvesting ability, thus improving carrier separation efficiency. Combining this with a different distinctive core and shell wall thickness would enhance the electron and hole pair separation in coupled heterostructures through forming an interface potential and effective charge separation.

In this work, we present a strategy for the fabrication of ZnO–ZnS core–shell NFs with different controlled shell wall thicknesses and study their catalytic activity through influencing the shell wall thickness. These core–shell NFs can be assembled in different ways enabling the construction

of nano-engineered device architectures with tailored functional properties. We demonstrate the highly sensitive visible photocatalytic properties of the ZnO–ZnS core–shell structures and that the catalytic efficiency is dependent on the shell wall thickness of the core–shell NFs. Our fabrication method involves electrospinning the metal oxide precursor and polymer composite fibers that serve as sacrificial templates for the subsequent annealing that precedes the formation of metal oxide (ZnO) NFs. Finally, through the sulfidation process, a shell layer (ZnS) is formed over the core ZnO NFs. Among the controlled strategies for producing NFs of inorganic materials, electrospinning offers several advantages, including ease of fabrication and versatility.[31]

Experimental section

Materials

Polyvinyl alcohol (PVA, MW: 125 000, Scientific Polymer), zinc acetate dihydrate (Sigma-Aldrich), thioacetamide (98%, TAA, Alfa Aesar), methylene blue (MB, Sigma-Aldrich), rhodamine B (RhB, Sigma-Aldrich), 4-nitrophenol (99%, 4-NP, Alfa Aesar), *p*-benzoquinone (98%, BQ, Alfa Aesar), triethanolamine, (99%, TEOA, Sigma-Aldrich) and isopropyl alcohol (99.5% IPA, Sigma-Aldrich) were procured and used as received without any further purification.

Electrospinning of ZnO nanofibers

The electrospinning solution was prepared by dissolving polyvinyl alcohol (PVA, 7.5% w/v) in water at 80 °C followed by the addition of zinc acetate dihydrate (4%, w/v). The resulting solution was stirred for 2 hours to obtain a homogeneous solution. Subsequently, the solution was loaded into a 3 mL plastic syringe with a needle diameter of 0.8 mm and placed horizontally in a syringe pump (KD Scientific, KDS101). The flow rate of the polymer solution was controlled using the syringe pump and was fixed at 0.5 mL h^{-1}. The grounded metal collector was covered with aluminum foil and placed at a distance of 12 cm from the needle tip. The electric field (15.0 kV) was applied from a high voltage power supply (Spellman, SL series, USA). The electrospinning procedure was carried out at 22 °C and 19% relative humidity in a Plexiglas box. The obtained zinc acetate/PVA composite NFs were further calcined at 400 °C for 3 h in air to obtain ZnO NFs.

Fabrication of ZnO–ZnS core–shell nanofibers

Shell wall controlled ZnO–ZnS based core–shell NFs were synthesized *via* a controlled sulfidation process. The conversion of the electrospun ZnO NFs to ZnO–ZnS core–shell NFs was carried out by immersing a ZnO NF web in 30 mM TAA solution at 60 °C in a water bath for different sulfidation times (0.5–9 h) to create different thicknesses of ZnS shell wall layer around the ZnO NFs. The creation of a ZnS shell layer over the ZnO surface materializes through a sulfidation process.[32] Finally, after different sulfidation reaction times, the samples were washed with distilled water and then dried at room temperature and annealed for 2 h at 200 °C in a vacuum oven.

Characterization

The morphological and elemental composition analyses were performed using a field emission scanning electron microscope (FESEM, Quanta 200 FEG) equipped with an energy dispersive X-ray spectrometer (EDS). The crystal structures of the annealed ZnO samples were observed using a PANalytical X'Pert multipurpose X-ray diffractometer with Cu Kα radiation. The core–shell forms of the NFs were imaged using transmission electron microscopy (TEM, FEI-Tecnai G2 F30), where the sample was dispersed in ethanol and a tiny droplet was cast and analyzed using a holey carbon coated TEM grid. TEM-EDX spectra were also recorded for samples sulfidated for 180 min. X-ray photoelectron spectroscopy (XPS, Thermo K-alpha-monochromated) was employed to analyze the surface chemical composition. UV-vis diffuse reflectance spectra were measured at room temperature over the 200–800 nm wavelength range using a Shimadzu UV-3600 spectrophotometer. Photoluminescence (PL) measurements were obtained using a time-resolved fluorescence spectrophotometer (FL-1057 TCSPC). The absorbance spectra of organic pollutants were obtained using a UV-vis spectrophotometer (Varian Cary 100).

Photocatalytic performance

The catalytic performances of the electrospun ZnO NFs and the shell wall controlled ZnO–ZnS core–shell NFs were evaluated by measuring the degradation of methylene blue (MB) dye under UV irradiation (Ultra-Vitalux Ultraviolet high pressure lamp (300 W, Osram, sunlight simulation)) and visible irradiation (75 W, Osram, xenon lamp with UV filter) at room temperature. Typically, 1 mg mL^{-1} samples of the electrospun ZnO based structures were placed into quartz cuvettes containing MB dye solution (10 ppm), which were then placed in the dark for 20 minutes to establish the adsorption/desorption equilibrium of the dye on the sample surface prior to irradiation. The samples were placed at a working distance of 15 cm from the lamp. A series of samples and controls (without catalyst) were simultaneously irradiated. The degradation of MB dye was monitored by measuring the absorbance as a function of irradiation time at predetermined time intervals using a UV-vis spectrophotometer. The reusability of the samples was tested for five consecutive cycles. The degradation efficiency toward MB dye was calculated using the formula $((C_0 - C)/C_0) \times 100$, where C and C_0 indicate the absorption peak intensities before and after UV irradiation. The same procedure was followed for Rh B (10 ppm) and 4-NP (10 ppm).

Active species trapping and superoxide radical quantification experiments

To identify the active species during the photocatalytic reaction, hydroxyl radicals ($^{\bullet}OH$), superoxide radicals ($O_2^{\bullet}$) and holes (h^+) were investigated by adding 1.0 mM isopropyl

alcohol (IPA) (a quencher of $^{\cdot}OH$), benzoquinone (BQ) (a quencher of $O_2^{\cdot}$) and triethanolamine (TEOA) (a quencher of h^+), respectively.[33,34] The method was similar to the aforementioned photocatalytic activity tests.

Results and discussion

Fig. 1 shows a schematic diagram of the procedure for preparing shell wall controlled ZnO–ZnS core–shell NFs through a combination of electrospinning followed by a sulfidation process. SEM images of the as-electrospun PVA/zinc acetate composite NFs clearly show the bead-free and smooth fibrous nature, with an average fiber diameter of 355 ± 85 nm, as shown in Fig. S1.† Furthermore, the as-prepared composite fibers were subjected to thermal treatment (calcination) for 3 h at 400 °C to form ZnO NFs, through totally degrading the organic part (the PVA polymer matrix and acetate groups). Annealing plays a vital role in determining the fiber morphology, which was clearly discussed in a previous publication.[35] The obtained ZnO NFs were subjected to a sulfidation process, which was studied with respect to reaction time. Our present study investigates the effect and role of the shell wall thickness of the ZnO–ZnS NFs on the effective visible photocatalytic properties. Clear indications can be sought from the representative SEM and TEM images exhibiting the entire structure and its associated morphological properties, as shown in Fig. 2 and 3. Post calcination, the fibrous surface turns rougher, as compared to the as-electrospun PVA/zinc acetate composite NFs. In short, it is apparent that the composition of the NFs is mainly ZnO nanograins, whose surface walls deform to ZnS under a sulfidation process. After annealing at 400 °C, the nanofibers (diameter of 180 ± 50 nm) show dense packing of small grains of size 35 ± 10 nm, as shown in Fig. 2a. It is found that the grains are bound to each other throughout the fiber and exhibit a solid morphology. Fig. 2b–f show SEM images of NF samples obtained after sulfidation times between 30 min and 540 min, which clearly demonstrate the change in the surface morphology of the

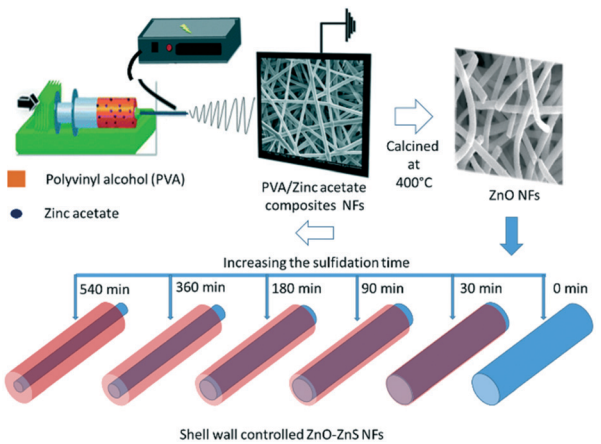

Fig. 1 Schematic diagram of the procedure for preparing shell wall controlled ZnO–ZnS core–shell NFs through a combination of electrospinning followed by a sulfidation process.

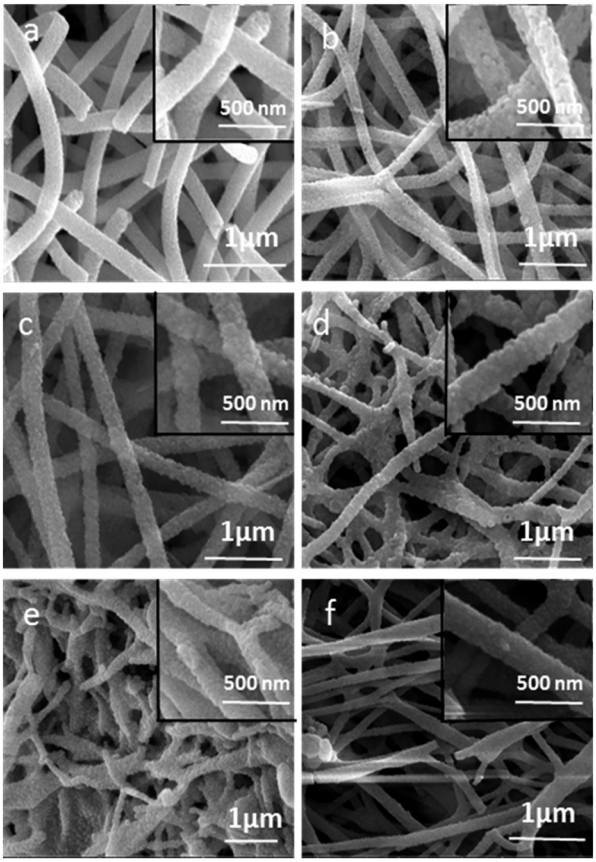

Fig. 2 Representative SEM images showing top views and highly magnified views (inset) of ZnO–ZnS NFs after different sulfidation times. (a) Pristine ZnO NFs at 0 min, (b) ZnO–ZnS NFs at 30 min, (c) ZnO–ZnS NFs at 90 min, (d) ZnO–ZnS NFs at 180 min, (e) ZnO–ZnS NFs at 360 min, and (f) ZnO–ZnS NFs at 540 min.

NFs with respect to the sulfidation time. Compared to the pristine ZnO NFs, noticeable surface roughness on the sulfidated samples implies that ZnS was decorated over the surface of the ZnO NFs. From Fig. 2b–f, it can be observed that up to a sulfidation time of 540 min, there is a considerable increase in the surface roughness with larger grains, but no break up or destructive change in the morphology of the NFs is present. The EDAX spectra of the ZnO NFs sulfidated for 30 min and 180 min reveal that the ZnS nanograins were functionalized over the ZnO NF surfaces (Fig. S2a and b†) and in terms of increasing reaction time, the sulfur ratio also increased. But upon prolonging the sulfidation time above 540 min (Fig. S3†), the fiber morphology was damaged and the NFs are converted into nanograins. The formation mechanism of the ZnO–ZnS core–shell NFs can be explained *via* the Kirkendall process, which normally refers to comparative diffusive migrations among different atomic species in metals and/or alloys under thermally activated conditions.

Fig. 3 shows TEM images of single NFs of pristine ZnO and shell wall controlled ZnO–ZnS after 90 min, 180 min and 540 min of sulfidation. The TEM images in Fig. 3a–d show detailed information about the interface between the ZnO core and the ZnS shell after different sulfidation times. The

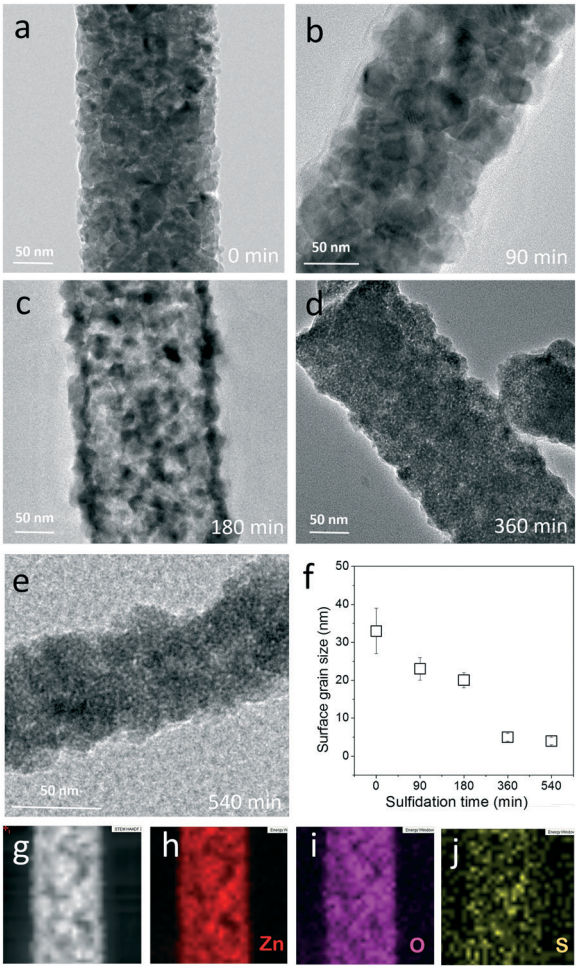

Fig. 3 TEM images and EDAX patterns of ZnO–ZnS core–shell NFs. TEM images of (a) ZnO, (b) ZnO–ZnS sulfidated for 90 min, (c) ZnO–ZnS sulfidated for 180 min, (d) ZnO–ZnS sulfidated for 360 min, and (e) ZnO–ZnS sulfidated for 540 min. (f) The average grain size measured from the TEM micrographs. The error bars indicates the diameter of the particle size distribution. (g–j) EDAX mapping results for ZnO–ZnS core–shell NFs sulfidated for 180 min.

contrast difference at the center and at the edges of the NFs confirms the core–shell structure. On increasing the sulfidation time, the shell wall thickness increases to ~5 nm, and ~20 nm after 90 min and 180 min of sulfidation, respectively (Fig. 3b and c). The sharp interface between the core and shell after 180 min of sulfidation clearly shows that the ZnO NFs are fully sheathed by a ZnS layer along their entire length. On further increasing the sulfidation time, ZnS shell layer conversion increases and the surfaces are completely modified with a nanograined (4–6 nm) shell wall (Fig. 3d). On further increasing the sulfidation time, the larger grained ZnO core completely deforms to ZnS nanograins, which favors the formation of ZnS NFs. But because of the assembly of the accomplished nanograined shell wall, the fiber morphology starts to deform, which is revealed by the decrease in the diameter of the nanofibers (Fig. 3e). It is revealed that after longer sulfidation times, the deformed ZnS nanograins are released from the fiber morphology. The measured mean grain diameters at the fiber surface plotted against sulfidation times are shown in Fig. 3f, demonstrating that larger ZnO grains (30 nm) were converted to ZnO nanograins (5 nm) and the transformation increased with respect to time. It can be noticed that the shell layer is not continually smooth; rather it is a formation of polycrystalline grains of ZnS, as can be seen from the HRTEM image. Although lattice distortion in ZnO and stacking faults in ZnS can be observed along the interface, both the core and shell exhibit lattice fringes and can be further identified as having wurtzite and hexagonal structures, respectively, thus indicating that the ZnS shell layer is decorated over the ZnO core. To confirm the presence of an outer ZnS shell layer, EDAX elemental mapping analysis was employed across a single core–shell NF sulfidated for 180 min, and is shown in Fig. 3(g–j). The EDAX mapping profile illustrates the presence of a higher S concentration on the surface of the ZnO NFs, and it reveals the successful formation of a ZnO–ZnS core–shell structure.

To get more information about the growth relationship, magnified HRTEM images of the core and shell were taken for the ZnO–ZnS NFs, and are shown in Fig. 4 for the pristine sample and for samples sulfidated for 180 and 540 min, respectively. The clear lattice spacing difference in the HRTEM images (Fig. 4) reveals that, after sulfidation, the outer

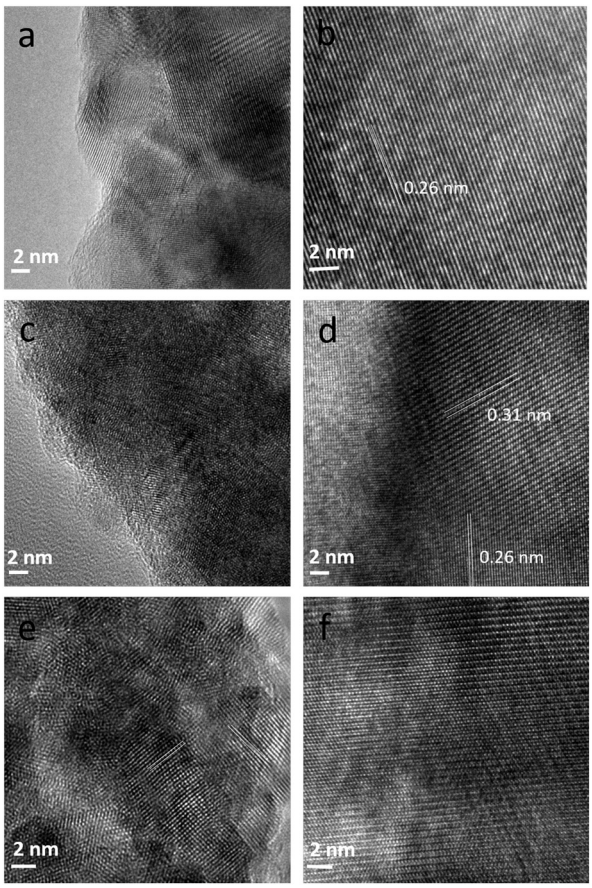

Fig. 4 HRTEM images of the core–shell interface and lattice spacing in (a and b) ZnO, (c and d) ZnO–ZnS sulfidated for 180 min, and (e and f) ZnO–ZnS sulfidated for 540 min.

surfaces of the NFs were deformed, as the ZnS nanograins have a lattice spacing of 0.31 nm.[36] Fig. 4c and d show that, after a shorter sulfidation time (180 min), the polycrystalline form of the ZnS nanograins coupled with the crystalline ZnO NFs gives rise to the formation of a ZnO–ZnS core–shell structural interface. The marked inter-planar d spacing of 0.31 nm corresponds to the (111) lattice plane of hexagonal ZnS with a (011) zone axis, and the *d* spacing difference of 0.26 nm corresponds to the ZnO nanograins. Contrary to this, for NFs sulfidated for longer times, the grains are found to be lesser in size with an incoherent arrangement. Importantly, it is found that the grains exhibit a strong polycrystalline nature, as they most likely exist monolithically with a size of around 5 nm. Moreover, it is noticed that the ZnS grains are pragmatically found in the form of individual nanograins, loosely bound to each other without a secondary particle arrangement.

XRD spectra of ZnO NFs and ZnO–ZnS core–shell NFs prepared under different sulfidation times are shown in Fig. 5a–f. Curve a shows the typical diffraction peaks of strong hexagonal ZnO (100), (002) and (101) (JCPDF no. 36-1451) at 2θ = 31.4, 34.2 and 36.3 respectively for pristine ZnO NFs, indicating a strongly preferred wurtzite (WZ) hexagonal structure before reaction with TAA solution. Fig. 5b–f present XRD patterns of ZnO–ZnS core–shell NFs synthesized with sulfidation times increasing from 30 min to 540 min. In the case of ZnO–ZnS core–shell NFs, the relative intensities of the peaks corresponding to ZnO are found to reduce due to the formation of an outer ZnS shell. Additional peaks corresponding to the lattice planes of the hexagonal (002) structure of ZnS are also observed in the XRD data. When the sulfidation time is 90 min, the diffraction peak of ZnO is still very strong, with a very weak peak of hexagonal ZnS (JCPDS 36-1450), as demonstrated in curve c. As the sulfidation time is increased to 180 min, the ratio of the characterization peaks of ZnS/ZnO increases (curve d), implying that more and more ZnO converts to ZnS with increasing reaction time. It is also noticed that the relative intensity of the ZnS related peak increases upon increasing the sulfidation time. This indicates that outer shell layers are getting thicker upon increasing the sulfidation time.

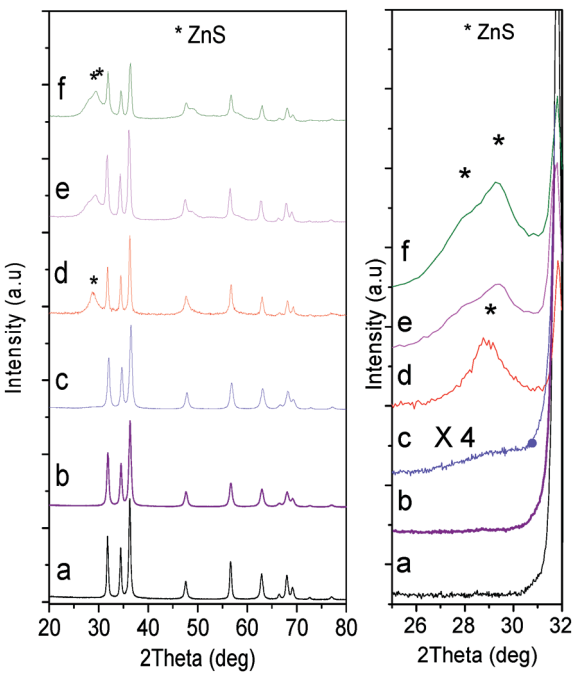

Fig. 5 XRD spectra of ZnO–ZnS core–shell NFs, for different sulfidation times. (a) Pristine ZnO (b) ZnO–ZnS after 30 min of sulfidation, (c) ZnO–ZnS after 90 min of sulfidation, (d) ZnO–ZnS after 180 min of sulfidation, (e) ZnO–ZnS after 360 min of sulfidation, and (f) ZnO–ZnS after 540 min of sulfidation.

On further increasing the sulfidation time over 540 min, most of the characterization peaks of ZnO get reduced and prominent nanocrystalline diffraction peaks of ZnS can be found in the XRD pattern of the final product (Fig. S3b†), demonstrating that on the surface, ZnO is completely converted to ZnS nanograins. No additional diffraction peaks other than those from ZnO and ZnS are observed in the XRD patterns, as the conversion of ZnO to ZnS is a diffusion limited process. But from the XRD results, it is clearly observed that the intensity ratio of the peak from the (002) plane of ZnS to the peak from the (100) plane of ZnO gradually increases with an increase in the reaction time. During the sulfidation process, sulfur diffuses into the ZnO lattices to occupy the oxygen vacancies. The ratio of the ZnS/ZnO peak intensity increased gradually when the sulfidation time was extended to 540 min, indicating that more ZnO was transformed into ZnS with increasing sulfidation time. Because the peaks from the (110) and (112) crystal planes of ZnS are close to the peaks from the (102) and (110) crystal planes of ZnO, these peaks may overlap.[37] The preferred orientation of the ZnO crystal facet through all conversion stages implies that the conversion from ZnO to ZnS takes place on the surface of ZnO columns and continues across the sidewall of the fibers.

Fig. S4a† shows UV-vis absorption spectra of ZnO and shell wall controlled ZnO–ZnS core–shell NF samples. For the as-prepared ZnO NFs, the spectrum has strong absorbance only in the UV range. When loading ZnS shell layers over the surfaces of the ZnO NFs, the band edge absorption red shifted towards the visible region as a function of sulfidation time. In comparison, increasing the shell layer thickness promotes the absorption towards the visible region compared with pristine ZnO NFs, and ZnO NFs sulfidated for 90 min show promising visible absorption behavior compared to the rest. The *K–M* plot reveals a change in band gap with the functionality of ZnS over the ZnO fiber. Fig. S4b† shows respective optical images of the ZnO and ZnO–ZnS NFs. Following the sulfidation process, the formation of the ZnS shell layer induces a color change to pale greenish, compared to a pristine white color.

Fig. 6 shows photoluminescence spectra of shell wall controlled ZnO–ZnS NFs. The band excitonic emission is clearly based on the presence of defect sites on the hierarchical surfaces of the NFs. Deconvolution of the spectra shows the

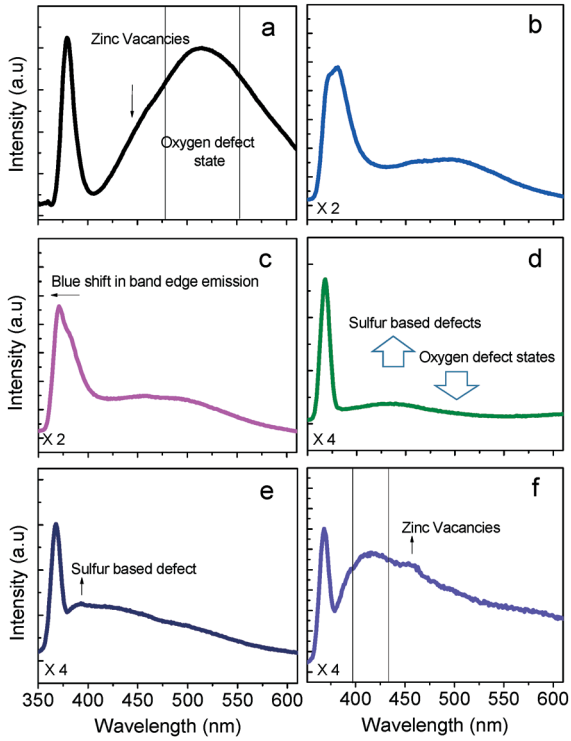

Fig. 6 Deconvoluted photoluminescence spectra of shell wall controlled ZnO–ZnS NFs synthesized using different sulfidation times: (a) 0 min, (b) 30 min, (c) 90 min, (d) 180 min, (e) 360 min, and (f) 540 min. The observed broad emission in the visible range confirms the presence of defects in ZnO with sulfur based impurities.

strong influence on ZnO photoluminescence of the shell layer interface and origin of the defect sites. The presence of defects has been confirmed by the broad range of defect emission in the visible region. Two prominent emitting bands, including a strong violet emission centered at around 380 nm and a broad green band centered at around 550 nm, are observed in the ZnO NFs. The green emission could be attributed to defect related emissions between Zn_i and the VB; O_{Vo} and the VB respectively, and the sharp emission at 380 nm represents the band edge emission of the ZnO NFs. The PL spectra of shell wall controlled ZnO–ZnS core–shell NFs reveal a decrease in the band edge emission, with the disappearance of the green emission and enhanced broad bluish emission compared to pristine ZnO NFs. The dominant peak in the UV range, which denotes the near band edge emission (NBE), is related to the direct recombination of photo-generated carriers, and has been classified as free excitonic emission and bound excitonic emission.

As a function of shell layer thickness, there is a slight shift in the NBE spectra towards shorter wavelengths as compared with pristine ZnO NFs, due to the removal of surface defect sites. The blue-shift in the UV emission can be attributed to the strain caused by lattice mismatch between ZnO and ZnS, and the removed surface defects increased the possible free excitonic emission from the ZnO NFs. As predicted by previous theoretical works, the strain in the ZnO–ZnS interface is strong enough to reduce the total band gap of the system.[24] The broad emission in the visible region observed for the ZnO–ZnS structures could be the superposition of two individual emissions from the core–shell structure. Along with the green emission (from ZnO), an additional peak in the bluish region (420 nm) could be associated with the ZnS layer. From observation and previous investigations, it is clear that Zn and V_O defects are dominant in the prepared electrospun ZnO NFs, and are apparently visible in the greenish band regions.[35] On performing a comparative analysis as a function of ZnS shell wall thickness, it is observed that the intensity of defect level emissions gradually decreases from the oxygen based defect sites, emphasizing the replacement of sulfur sites in the fiber network. The promotion of sulfur based defect emission in the bluish region clarifies the presence of a ZnS layer over the ZnO nanofibers with a significant reduction in oxygen defect related emission in the core–shell system. In addition, it is also noticed that the intensity of sulfur based defect emission becomes intense as a function of increasing sulfidation time.

Moreover, wide band gap ZnS as a shell layer over the surface of ZnO passivates the surface electronic states of ZnO NFs, resulting in an obvious enhancement in UV luminescence. A broad peak at ~425 nm arises as an outcome of sulfidation, resulting from respective radiative recombination on the surface of ZnS nanograins with sulfur vacancies.[38] Therefore, the successful combination of both core–shell structures influences the luminescent properties, which leads to the development of interesting facts about defect engineering in electrospun ZnO nanostructures. The violet and blue emissions are attributed to transitions from IZn (IZn → the VB) and extended IZn states (Sul defect → VZn) to the valance band, respectively.[39] Apparently, upon increasing the sulfidation time, the intensities of violet and blue emissions are increased, whereas the greenish emission is suppressed. Importantly, the peak positioned at ~443 nm corresponds to the blue emission, which is significantly red-shifted to 461 nm upon increasing the sulfidation time, due to the removal of Zn interstitial defects *via* sulfur interactions, which favor the transition of electrons from the CB → VZn. This clearly evidences the transformation of ZnO to ZnS, leading to the removal of Zn interstitials in the core–shell system. All the hierarchical samples show superior UV emission, denoting the good optical quality of the NF structures.

As a result, more photo-generated electrons and holes are confined inside the ZnO core, giving rise to a high quantum yield about 4 times greater than that of the ZnO NFs alone. However, the green emission is weakened to a great extent. As we know, the green emission originates from oxygen interstitials and vacancies.[35] During the formation of ZnO–ZnS core–shell structures, the hydrolysis of TAA can produce H_2S and sulfur atoms can replace and squeeze out the oxygen interstitials and vacancies from the surfaces of ZnO nanocrystals. As a result, the concentration of oxygen interstitials is reduced greatly and the green emission is weakened. The above results indicate that the sulfidation process has a great

effect on the relative intensities and positions of typical PL emissions from ZnO nanocrystals. Therefore, the PL properties of ZnO nanocrystals could be tuned using this approach.

The Zn 2p, S 2p, and O 1s binding energies in the hierarchical photocatalysts were investigated using XPS to investigate the surface compositions and chemical states of the ZnO NFs as a function of sulfidation time, shown in Fig. 7. Fig. 7a shows high resolution scans of the O 1s profile spectra which are composed of multiple peaks with the Gaussian function with respect to sulfidation time. The three peaks fitted with the Gaussian function denote the existence of three different O species, namely lattice oxygen (O_L), oxygen vacancies (O_V) and chemisorbed oxygen species (O_{Ch}).[35] The peaks at 530.1 ± 0.2 eV in all samples are attributed to O^{2-} ions in the wurtzite structure of a hexagonal Zn^{2+} ion array, which are surrounded by zinc atoms with a full supplement of nearest-neighbor O^{2-} ions. This is generally known as lattice oxygen (O_L) and its percentage represents the relative amount of O at ideal lattice positions. The centred peak located at 531 ± 0.1 eV is attributed to O^{2-} ions in oxygen deficient regions within the matrix of ZnO. The third peak around 532.1 ± 0.2 eV is typically ascribed to OH^- groups, chemisorbed oxygen or dissociated oxygen on the surface of ZnO.

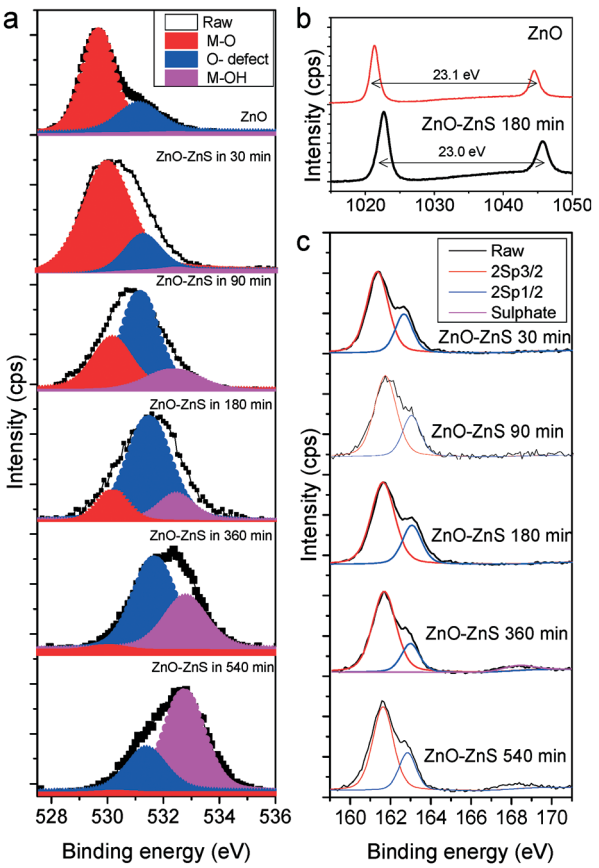

Fig. 7 XPS spectra of the (a) O 1s, (b) Zn 2p, and (c) S 2p states in sulfidated ZnO NF following different sulfidation times between 0 min and 540 min. The observed high resolution scans for the O 1s spectra are composed of multiple peaks and fitted as three peaks denoting the existence of three different O species, named lattice oxygen (O_L) (shaded in red), oxygen vacancies (O_V) (shaded in blue) and chemisorbed oxygen species (O_{Ch}) (shaded in magenta).

The observed variations in the intensities of the peaks might be connected to the concentration of oxygen vacancies due to the deformation of ZnS nanograins. The calculated relative percentages of O_L, O_{Ch} and O_V for all samples are noted in Table S1.† The highest intensity of O_L, compared to O_{Ch} and O_V, indicates the strong Zn–O bonding in the prepared samples. The gradual decrease in O_L observed in the sulfidated samples denotes that the lattice oxygens bound with Zn were deformed to a Zn–S bond as a result of sulfidation. It is realized that upon increasing the sulfidation time, the ratio of O_L decreases and the oxygen deficiency ratio is enhanced. Additionally, the significant ratio of the O_{Ch} peak, related to chemisorbed oxygen, is enhanced at longer sulfidation times, which reveals that the sites of oxygen ions were replaced with sulfur ions and the oxygen ions were removed from the zinc lattice. The estimated relative percentage of lattice oxygen (O_L) decreased with increasing sulfidation time. The intense characteristic peaks observed at 1021.5 ± 0.3 eV and 1044.6 ± 0.2 eV in the XPS spectra of Zn 2p are assigned to Zn $2p_{3/2}$ and Zn $2p_{1/2}$, respectively (Fig. 8b). The spin–orbit splitting of ~23.1 eV between the two core level components of Zn $2p_{3/2}$ and Zn $2p_{1/2}$ is in good agreement with reported literature values, which confirms their 2^+ state. After sulfidation, the binding energies are slightly higher than those of pristine ZnO and those reported for bulk ZnO (Table S1†), and they are closest to those reported for bulk ZnS, which evidences Zn–S bond formation.[40] The peaks depicted in Fig. 7c represent the S 2p signal in the core–shell heterostructures. The S 2p signal is split into two main components of different intensities: a higher intensity peak at 162.2 eV, attributed to S 2p, and a lower one at 168.8 eV, usually attributed to SO_4 2p. Moreover, the relative intensities of these peaks are completely different as a function of sulfidation time. The prominent S 2p peak deconvoluted at about 161.6 eV and 162.7 eV could be attributed to S $2p^{3/2}$ and S $2p^{1/2}$, which are ascribed to the hybrid chemical bond species of S^{2-} and Zn–S.[40] The S 2p peak is significantly more intense in the ZnO–ZnS heterostructures as compared to the sulphate peaks, with no trace of the presence of metallic (monoplasmatic) sulfur (284–285 eV) or the presence of C–S bonds in the core shell heterostructures (Fig. S5† and 7c). There is a possibility of C doping during the synthesis process, but the absence of a peak at 283.3 eV associated with Zn–C bonds connected to O_V reveals the absence of carbon doping in the ZnO NFs (Fig. S5†).[41] Altogether, these results confirm the presence of a ZnS phase at the outer surface of the produced ZnO NFs and, upon increasing the sulfidation time, the presence of sulphate functionality increases due to the effective deformation of ZnO to ZnS. Classical peak fitting of the high resolution S 2p XPS spectra of the heterostructured NFs gives an oxidation ratio that increases with the sulfidation time (Table S1†).

Electrospun nanofiber based catalytic systems display enhanced photocatalytic performances owing to the existence of

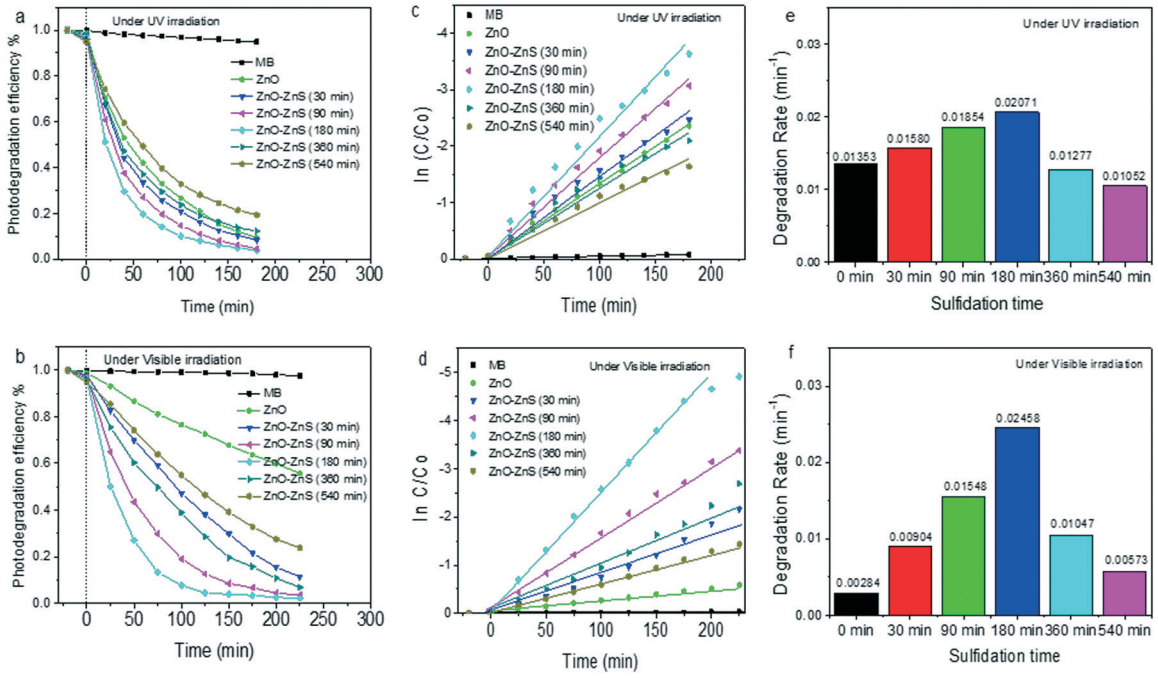

Fig. 8 Photocatalytic properties of shell wall controlled ZnO–ZnS core–shell NFs. (a and b) Photocatalytic degradation efficiencies and (c and d) kinetic fits for ZnO–ZnS NFs under UV irradiation and visible irradiation, and (e and f) a comparative study of the photocatalytic degradation rates under UV irradiation and visible-light irradiation for ZnO–ZnS core–shell NFs.

larger surface areas and other dominant features.[40] Fig. 8 displays the photodegradation efficiencies of as-prepared ZnO NFs and different shell wall thickness grown ZnO–ZnS core–shell NFs towards MB under simulated UV and visible sources. Recorded absorption spectra of MB as a function of irradiation time during the degradation processes are presented in Fig. S6.† The self-degradation efficiency of the control dye solution without any catalyst is also presented for comparison and is found to be ~7% under irradiation for 180 min. As shown in Fig. 8a, ZnO–ZnS core–shell nanostructures exhibited MB decomposition levels of 84.64%, 87.37%, 93.78%, 91.89%, 83.55%, and 75.51% for the ZnO NFs and ZnO–ZnS NF core–shell morphologies sulfidated for 30 min, 90 min, 180 min, 360 min, and 540 min, respectively, under UV irradiation for 180 min. Fig. 8b shows that upon irradiating the ZnO based nanostructures with visible light, they exhibited MB decomposition levels of 32.27%, 70.21%, 91.58%, 96.23%, 80.42% and 60.87% for ZnO NFs and ZnO–ZnS NF core–shell morphologies sulfidated for 30 min, 90 min, 180 min, 360 min, and 540 min, respectively, after 225 min. Table S2† records the photoresponsive properties of shell wall controlled ZnO–ZnS based core–shell NFs. Pristine ZnO NFs may have mild degradation activity of around 32% due to the presence of defect states which promote catalytic behavior under visible response.[42] Compared to bare ZnO NFs, ZnO–ZnS based core–shell NFs sulfidated for 180 min show higher visible catalytic activity. It is also shown that the photocatalytic activity of the hybrid nanostructures first tends to increase and then decreases with an increase in the thickness of the ZnS shell layer. ZnO–ZnS core–shell NFs having a shell wall thickness of ~20 nm synthesized with 180 min of sulfidation show the maximum photocatalytic efficiency, indicating that shell wall thickness is critical for enhancing the catalytic performance. The superior photocatalytic performance of these hybrid structures may be explained as follows. Similar to the catalytic activity, the optical response was enhanced depending on the shell wall thickness, which was confirmed from the UV and PL results (Fig. S4† and Fig. 6).

During the charge transfer process in ZnO–ZnS hybrid structures, the conduction band of ZnS lies at a more negative potential than that of ZnO, while the valence band of ZnO is more positive than that of ZnS. Under photo-irradiation, photogenerated electrons pass from the conduction band of ZnS to the corresponding band of ZnO and hole transfer occurs from the valence band of ZnO to that of ZnS. Simultaneous yield and the lifetime of charge carriers were increased in the ZnO–ZnS system by effective electron and hole transfer, resulting in the formation of highly oxidative hydroxyl radical species ($OH^{\bullet}$) and super oxide ions ($O_2^{\bullet}$). At the same time, MB degradation experiments were conducted in the presence of ZnO and sulfidated ZnO NFs under dark conditions and the respective absorbance spectra (Fig. S7†) clearly demonstrate that there is no notable degradation observed up to 240 min. But when compared to the ZnO NFs, the sulfidated ZnO NFs have adsorbed 6.7% of dye molecules under the equilibrium state. This confirms that the dye molecules were highly interactive with the core–shell catalytic system compared to the pristine one. The experimental data in Fig. 8(a and b) can be well fitted to a pseudo first-order

kinetics equation. Fig. 8(c and d) shows kinetics plots of shell wall controlled ZnO–ZnS core–shell NFs for the MB photo degradation reaction. Upon varying the ZnS wall thickness, the plot of $\ln(C/C_0)$ against irradiation time (t) is nearly a straight line, in which the slope of the fitting line is equal to the value of the rate constant. The corresponding kinetic constants for different shell wall controlled NFs under UV and visible irradiation are shown in Fig. 8e and f respectively.

Under visible irradiation, the highest apparent rate constant under our experimental conditions is determined to be 0.02458 min^{-1} for ZnO–ZnS core–shell NFs sulfidated for 180 min, having a shell wall thickness of 20 nm, which is about 9 times and 4 times higher than for pure ZnO NFs (0.00284 min^{-1}) and ZnS (sulfidated for 540 min) NFs (0.00573 min^{-1}) respectively, revealing the superior visible photocatalytic activity of core–shell hierarchical NFs. But the trend of photocatalytic properties was not similar under UV and visible irradiation for different thicknesses of shell wall controlled ZnO–ZnS NFs. Under UV irradiation, ZnO–ZnS NFs sulfidated for 30 min show a faster degradation rate compared to ZnO–ZnS NFs sulfidated for 360 min, but under visible irradiation this was reversed. This happens because under UV irradiation, the ZnO core NF acts as a promising catalyst and the removal of oxygen related surface defects favors the effective carrier separation rate in the sulfidated samples. On increasing the sulfidation time, the removal of oxygen related defects with the presence of sulfur based defect states favors carrier separation efficiency, which enhances the catalytic efficiency. But under visible irradiation, the core–shell interface and sulfur induced defects play a major role in improving the catalytic efficiency, which is due to the lack of a core shell interface in the shorter sulfidation time (30 min) samples. The degradation rate is slower compared with the ZnO–ZnS NFs sulfidated for 360 min, which have a promising core shell interface with a high number of sulfur based defect states. Additionally, the core–shell based heterostructures have a higher adsorption ratio compared with the pristine ZnO NFs, revealing more interactions between the deformed surfaces and the dye molecules than for the pristine ones. This may be due to the chemisorbed oxygen sites on the surfaces of the core–shell structures, which was confirmed through the XPS results. These would be more advantageous in enhancing the dye degradation process since the presence of hydroxyl groups can effectively facilitate the trapping of photoinduced electrons and holes. Furthermore, the photocatalytic degradation efficiencies of pristine and highly efficient ZnO–ZnS core–shell heterostructure toward Rh B and 4-NP were studied and the results are shown in Fig. 9. The decolourization of pollutants was evaluated through monitoring the absorption spectra, as shown Fig. S8 and S9.† It is noted that the heterostructured catalyst effectively degraded the selected organic pollutants under visible irradiation. Corresponding digital images of pollutants taken at definite time intervals are shown in Fig. 9b. The degradation efficiencies of ZnO

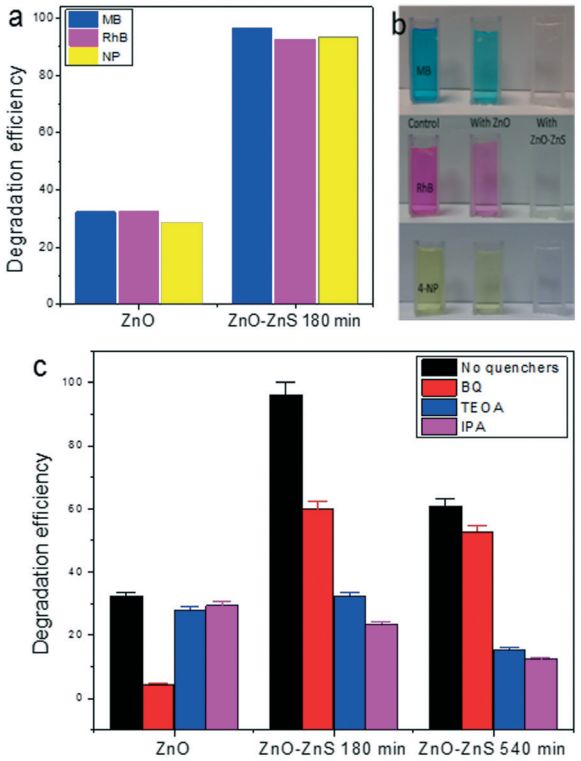

Fig. 9 (a) The catalytic efficiency of the core–shell heterostructures toward MB, Rh B and 4-NP, and (b) digital photographs of MB, Rh B and 4-NP in the presence of ZnO and ZnO–ZnS core–shell NFs under visible irradiation before and after 140 min of irradiation. (c) Trapping experiments with active species during the photocatalytic reaction following 140 min of Xe lamp irradiation.

and the ZnO–ZnS core–shell heterostructures for Rh B and 4-nitrophenol were calculated to be ~22% and ~28% after 140 min, and ~93% and 85% after 140 min, respectively, under visible irradiation. There is the possibility of dye sensitization effects while using MB and Rh B dyes under visible irradiation, but the exhibition of similar catalytic degradation rates for NP degradation as compared to for dye molecules shows that the degradation efficiency was not influenced much by the dye sensitization effect. Additionally, the degradation performance toward colorless pollutants such as 4-chlorophenol provides evidence for the exclusion of dye sensitization effects and denotes visible catalytic behavior of the heterostructured interface of ZnO–ZnS core–shell NFs (Fig. S10†).

The significantly enhanced photocatalytic activity of the hybrid composite catalysts motivates us to further study the photocatalytic reaction mechanism of the degradation process. Diverse feasible mechanisms, including the production of reactive oxygen species involved in the enhancement of the photocatalytic activities, were investigated by quantifying the production of reactive oxygen species in the reactive medium (Fig. S11†). Fig. 9c displays trapping experiments of active species during the photocatalytic reaction of ZnO–ZnS core–shell NFs under visible irradiation. Generally, photo induced holes (h^+), hydroxyl radicals ($^{\bullet}OH$) and superoxide

radicals ($^{\cdot}O_2$) are known to be the main reactive species involved in photodegradation reactions. In our radical trapping experiments, 1 mmol L^{-1} of isopropanol (IPA), 1,4-benzoquinone (BQ) and triethanolamine (TEOA) were added into the solution and used as hydroxyl radical, superoxide radical and hole scavengers, respectively, and their influence on the photocatalytic degradation efficiency toward MB is shown in Fig. 9c. For pristine pure ZnO NFs, the photocatalytic degradation activity toward MB decreases remarkably with the addition of BQ. However, when IPA and TEOA are added, the activity declines, but not as significantly as with BQ addition. These results suggest that the production of superoxide radicals in ZnO is majorly responsible for the catalytic activity. For ZnO–ZnS core–shell NFs sulfidated for 180 min and 540 min, the photocatalytic degradation activities toward MB decreased remarkably upon the addition of IPA and TEOA. However, when BQ was added, there was no significant decrease in catalytic activity on the NFs sulfidated for 540 min but those sulfidated for 180 min were influenced by BQ. These results suggest that under visible light irradiation, the shell wall controlled ZnO–ZnS core–shell NFs follow a similar photocatalytic mechanism for the degradation of MB, in which the holes and hydroxyl radicals play a more major role than the superoxide radicals. Thus, both holes and hydroxyl radicals are the primary active species in this reaction. Moreover, compared with ZnO NFs sulfidated for 540 min, the photodegradation efficiency of ZnO–ZnS core–shell NFs sulfidated for 180 min declines more significantly with the addition of IPA and TEOA, indicating that more hydroxyl radicals and holes may exist in the ZnO–ZnS system on the surface than in the ZnS system, due to the effective separation of photogenerated carriers.

Based on the above experimental results, a possible mechanism has been proposed for the enhanced visible-light activity of ZnO–ZnS hierarchical core–shell catalysts and a schematic diagram is illustrated in Fig. 10. The significant improvement in the photocatalytic performance can be ascribed to the synergistic effect between the ZnO core and ZnS shell. The band gaps of ZnO and ZnS are 3.2 eV and 3.5 eV, respectively, but both pure samples can't be excited by visible light and thereby produce photoinduced electrons and holes. But constructing a ZnO–ZnS core–shell form of nanostructure could exhibit visible catalytic ability due to the creation of a ZnS–ZnO interface, which leads to a narrower band gap than for individual ZnS and ZnO.[43] Previously, Schrier *et al.* have predicted that conduction band energies are reduced for ZnO and ZnS while designing ZnO–ZnS core–shell forms of nanowires, and that the overall band gap of ZnO–ZnS is lowered to 2.07 eV due to strained conduction band minimum (CBM) energies.[44] Designing a monolayer of ZnS on the ZnO surface would increase its work function and contribute to the band bending and surface dipole movement due to the electronic

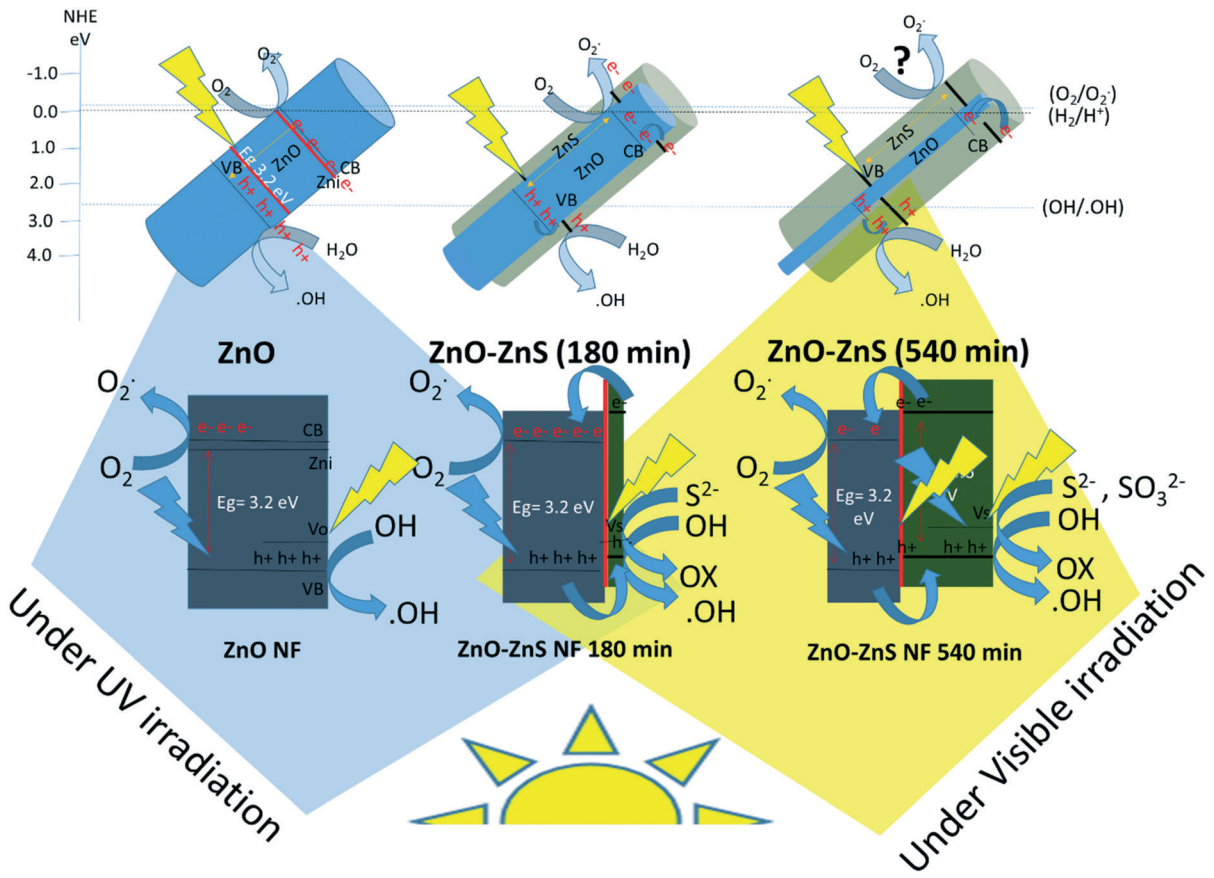

Fig. 10 Schematic representation of the photocatalytic mechanism in varied shell wall thickness ZnO–ZnS heterostructural photocatalysts.

hybridation of the ZnO band structure with the surface states induced by the ZnS monolayer.[45] Further, Wang *et al.*[46] have proven that the creation of ZnS based surface states on a ZnS–ZnO based heterostructure would influence the band bending and effectively reduce the band function at the ZnO–ZnS interface. And the population over the ZnS based surface states would be the crucial factor for the visible photocatalytic behaviour. In our work, HRTEM images (Fig. 3 and 4) exhibit the presence of ZnS nanograins on the ZnO NFs, and as a function of sulfidation time, ZnO NFs were completely surrounded by ZnS nanograins, creating a ZnO–ZnS interface which will lead to a narrow band gap at the core shell interface. And the presence of sulfur based defect states increased upon increasing the sulfidation time, favouring visible absorption and the effective separation of charge carriers. As observed from the PL and XPS spectra (Fig. 6 and 7), there is the presence of ZnS based surface states, which were favourable for the visible response and improve the visible catalytic behaviour. At the core shell interface, ZnS based surface states facilitate electron–hole separation by acting as photo-generated hole trappers.[46] But the presence of sulfur based defect states throughout the shell layer may improve the carrier recombination rate and delay carriers from reaching the catalytic surface which will reduce the effective radical production and delay the catalytic efficiency in thicker shell wall grown ZnO–ZnS core shell NFs.

The photocatalytic performance of a semiconductor is dependent on the production of photo-induced charge carriers and the production of reactive oxygen species which are determined by the light harvesting ability. In ZnO–ZnS core–shell arrays, both the bottom of the conduction band (CB) and the top of the valence band (VB) of ZnS (−0.96 eV and 2.84 eV *vs.* NHE, pH = 7) are more negative than in the ZnO core (−0.32 eV and 2.98 eV *vs.* NHE, pH = 7). Thus the photogenerated electrons could transfer easily from ZnS into the CB of ZnO, while the holes could migrate from ZnO into the VB of ZnS, *via* the interface of the heterojunction. This creates the redistribution of charge carriers on each side of the heterojunction (as shown in Fig. 10) which significantly hinders the recombination process of electron–hole pairs and improves the efficiency of interfacial charge separation. In addition, the photogenerated electrons in the CB of ZnO can improve the carrier mobility in the inner core and the photogenerated holes reduce the dissolved OH to yield abundant active $^{\bullet}$OH, together with holes in the VB of ZnS employed for further effective reduction of MB. Therefore, owing to the high transfer and separation efficiency of charge carriers in this heterojunction system, ZnO–ZnS core–shell NFs demonstrate superior photocatalytic performance compared with unmodified ZnO NFs.

On controlling the effective shell wall thickness of the ZnO–ZnS hierarchical core–shell NFs, the ratios of the effective separations of charge carriers are varied, which determines the catalytic performance of the NFs under visible irradiation. Modifying the surface of ZnO with a thin layer of ZnS initiates effective heterojunction formation and avoids surface defects of ZnO (confirmed from Fig. 7). It is well known that the electron affinities (E_a) of ZnO and ZnS are 4.5 and 3.9 eV, respectively.[47] Therefore, an upward band offset of 0.6 eV between the conduction bands of ZnO and ZnS exists in the energy band diagram of the ZnO–ZnS NFs (Fig. 10b). We believe that the spatial separation of the carriers reduces the recombination probability of the photogenerated electron and hole pairs. And the presence of ZnS based states at the core–shell interface favors photogenerated electron hole separation by acting as photo generated hole trappers.[46] Therefore, the photo-response of the ZnO–ZnS core–shell NF arrays significantly increases when compared with unmodified ZnO NFs, under illumination from UV and visible light.

An optimum shell thickness of around 20 nm shows the highest photocatalytic activity, which reveals that the photoresponsivity of the ZnO–ZnS core–shell NFs are controlled by the shell wall thickness. Since ZnS is in contact with the dye solution, the charges reaching the ZnS surface are responsible for the photocatalytic activity. On increasing the shell wall thickness above 20 nm, the catalytic performance starts reducing. This phenomenon can be due to the fact that the thick ZnS shell layer suppresses the tunneling of holes from the ZnO core to the surface atoms of the shell, resulting in the blockage of holes or the presence of a higher density of ZnS based defect states acting as carrier recombination sites. It should be notified that, under visible light (λ = 400 ± 15 nm) irradiation, the production rate of reactive oxygen species on the surface of the ZnS shell surface was reduced (Fig. 9). Thus, the photogenerated charge carriers in ZnO–ZnS core–shell NFs having a higher shell wall thickness take a longer time to reach the surface, which augments the recombination probability and decreases the catalytic efficiency. Thus, the best degradation activity toward MB is attained in samples having a shell wall thickness of ~20 nm. This indicates that, in this particular case, the structure after 180 min of sulfidation should give the ideal ZnO–ZnS core–shell structure which balances the charge separation and transport rates and hence is the most favorable sample for enhanced photocatalytic activity.

Reusable properties

The stability of photocatalysts upon light irradiation is very important. It is reported that semiconductor photocatalysts usually suffer from instability caused by photocorrosion over long-term photocatalytic reactions. Fig. S12† shows the catalytic degradation performances of recycled photocatalysts during five repeated tests. After being washed with water, ZnO–ZnS NF based immobilized photocatalysts can be recycled. Structural and morphological aspects are investigated and clearly evidence that hierarchical arrays are more stable after five consecutive recycling processes. During the five repeated degradation cycles, limited activity loss was observed for ZnO–ZnS NF based photocatalysts. The degradation efficiency rate for the fifth test was 92.6% that of the

first test. On further increasing the test to 10 cycles, the degradation efficiency rate was reduced to 62%. To attain an in-depth view on the effect of photo-corrosion on the catalyst, we have exposed electrospun ZnO nanostructures to photo-irradiation for a time period of 24 h, changing the dye solution and studying the changes in surface morphology and chemical composition.

The observed morphological features evidently reveal that the surface of the ZnO was influenced by structural damage, with a flake-like surface structure, as clearly shown in Fig. S13.† But the ZnO–ZnS based heterostructures had quite stable surface features as compared with pristine ZnO, without any significant morphological alteration and agglomeration. This reveals that the ZnS based shell layer acts as a protective layer and avoids photo-corrosion effects, as illustrated in Fig. S13.† But, it also mildly influences the photooxidation process by trapping holes, which initiates the formation of $ZnSO_4$ *via* the photo-corrosion effect, with changes in the surface features. In addition, high resolution XPS analysis of the samples proved a drastic shift in the O 1s peak to 533.97 ± 1.0 eV. Similarly, the intense characteristic peaks observed at 1021.5 ± 0.3 eV and 1044.6 ± 0.2 eV in Zn 2p were considerably shifted to 1023.3 ± 0.5 eV and 1046.35 ± 0.4 eV, respectively, as illustrated in Fig. S14.† The peak observed at 162 eV represents S^{2-} in the ZnS shell layer, and additionally there are mild traces of SO_3^- peaks around 169 eV in the highly active ZnO–ZnS core shell NFs. To study the outcome of the solubility and photo-corrosive effects on the ZnO–ZnS NFs, the presence of sulphate groups before and after the catalytic experiments was taken into consideration to detect the photo-oxidisation of ZnS–$ZnSO_4$. After photo-irradiation, additional intense peaks of SO_3^- were observed, as compared with the core–shell samples before irradiation as shown in Fig. S15.† The ratio of sulphide to sulphate is revealed to have significantly changed before and after the catalytic process through quantifying the atomic concentration. The presence of increments on the SO_3^- peak evidences the presence of $ZnSO_4$ after the catalytic process and signifies the corrosion effect. This evidences the photo-corrosion effect on the ZnO–ZnS core–shell NFs. But there is no significant shift in the ZnO–ZnS core–shell nanostructured surface states when compared with samples before photo-irradiation. The findings confirm the photocorrosion of ZnO during the photo degradation process, but also the minimal effect on the ZnO–ZnS core–shell structures. Further improvements in the inhibition of photo-corrosion in electrospun ZnO nanostructures present a challenge and more efforts are needed to provide a solution to this issue. The ZnO–ZnS core–shell NF based photocatalysts exhibited high visible photocatalytic activity and good stability. Moreover, it is imperative to clearly differentiate the effective role of the shell wall thickness on the ZnO NF surface, which effectively contributes to the visible photocatalytic behavior and effective charge separation. The formation of shell wall controlled ZnO–ZnS core–shell NFs favors the absorption of light and the separation of photogenerated electron–hole pairs, and contact between the reactant solution and the photocatalysts, leading to efficient photocatalytic activity. Interestingly, it should also be noted herein that a shell wall thickness of 20 nm promotes superior photodegradation performance compared to other structures under UV and visible irradiation, implying the crucial role of shell layer thickness in effective charge separation. In the current study, we have thus highlighted the creation of a shell layer with different thicknesses in order to engineer effective charge separation and improve visible absorption in electrospun ZnO NFs for better photocatalytic performance.

Conclusions

We have effectively demonstrated the visible photocatalytic properties of shell wall thickness controlled ZnO–ZnS core–shell NFs, formed through the deformation of electrospun ZnO NFs to core–shell heterostructural NFs, and their comparative degradation efficiency toward MB. The shell wall thickness and its effective charge separation efficiency were conceived as primary factors and the visible photocatalytic efficiencies of ZnO based nanostructures were evaluated. Furthermore, it was observed that the dense ZnO nanograins are deformed to ZnS nanograins during the sulfidation process, with a simultaneous increase in grain size. The thickness of the ZnS shell has a great influence on the photocatalytic performance of the ZnO–ZnS core–shell NFs, and the maximum degradation rate of the ZnO–ZnS based hierarchical photocatalysts reached 0.02071 and 0.02458 min^{-1} under UV and visible light irradiation. The degradation efficiency after the fifth recycling test is 92.6% that of the first test. It has been shown that ZnO–ZnS core–shell NF arrays having a shell wall thickness of 20 nm exhibit high photocatalytic activity and good stability during dye degradation. This implies the benefit of a detailed study on the effects of shell wall thickness promoting effective charge separation and improving visible absorption for the development of an efficient visible light active catalyst.

Acknowledgements

K. S. Ranjith and B. Balusamy acknowledge the Scientific & Technological Research Council of Turkey (TUBITAK), BIDEB 2216-Fellowships for Research Fellowship Programme for Foreign Citizens for postdoctoral fellowships. A. Senthamizhan acknowledges the TUBITAK BIDEB 2221 fellowship program for visiting scientists. T. Uyar acknowledges the Turkish Academy of Sciences – Outstanding Young Scientists Award Program (TUBA-GEBIP)-Turkey for partial funding.

References

1 N. G. Cho, D. J. Yang, M. J. Jin, H. G. Kim, H. L. Tuller and I. D. Kim, *Sens. Actuators, B*, 2011, **160**, 1468–1472.
2 Q. Li, Y. Xu, H. Wei and X. Wang, *RSC Adv.*, 2016, **6**, 65275–65281.
3 D. Chen, Z. Wang, T. Ren, H. Ding, W. Yao, R. Zong and Y. Zhu, *J. Phys. Chem. C*, 2014, **118**, 15300–15307.

4 Y. K. Hsu, Y. C. Chen and Y. G. Lin, *ACS Appl. Mater. Interfaces*, 2015, **7**, 14157–14162.
5 D. W. Lawrence, C. Tran, A. T. Mallajoysula, S. K. Doorn, A. Mohite, G. Gupta and V. Kalra, *J. Mater. Chem. A*, 2016, **4**, 160–166.
6 L. M. Colangelo and A. J. Baeumner, *Lab Chip*, 2012, **12**, 2612–2620.
7 J. Y. Chen, L. C. Zhu, Y. X. Xue, L. X. Shi and M. S. Cao, *Appl. Phys. Lett.*, 2008, **92**, 223101–223103.
8 F. Li, X. Gao, R. Wang, T. Zhang, G. Lu and N. Barsan, *ACS Appl. Mater. Interfaces*, 2016, **8**, 19799–19806.
9 S. H. Choi, G. Ankonina, D. Y. Youn, S. G. Oh, J. M. Hong, A. Rothschild and I. D. Kim, *ACS Nano*, 2009, **3**, 2623–2631.
10 S. Khanchandani, S. Kumar and A. K. Ganguli, *ACS Sustainable Chem. Eng.*, 2016, **4**, 1487–1499.
11 S. Hernández, V. Cauda, A. Chiodoni, S. Dallorto, A. Sacco, D. Hidalgo, E. Celasco and C. F. Pirri, *ACS Appl. Mater. Interfaces*, 2014, **6**, 12153–12167.
12 J. Schneider, M. Matsuoka, M. Takeuchi, J. Zhang, Y. Horiuchi, M. Anpo and D. W. Bahnemann, *Chem. Rev.*, 2014, **114**, 9919–9986.
13 S. Muthulingam, K. B. Bae, R. Khan, I. H. Lee and P. Uthirakumar, *RSC Adv.*, 2015, **5**, 46247–46251.
14 Q. Wen, J. Zhuang, Q. He, Y. Deng, H. Li and J. Guo, *RSC Adv.*, 2015, **5**, 91997–92003.
15 X. Zong, C. Sun, H. Yu, Z. G. Chen, Z. Xing, D. Ye, G. Q. Lu, X. Li and L. Wang, *J. Phys. Chem. C*, 2013, **117**, 4937–4942.
16 G. Zhang, Y. Wu, H. Ding, Y. Zhu, J. Li, Y. Lin, S. Jiang, Q. Zhang, N. Pan, Y. Luo and X. Wang, *RSC Adv.*, 2015, **5**, 71883–71889.
17 D. Hong, W. Zang, X. Guo, Y. Fu, H. He, J. Sun, L. Xing, B. Liu and X. Xue, *ACS Appl. Mater. Interfaces*, 2016, **8**, 21302–21314.
18 J. W. Jung, C. L. Lee, S. Yu and I. D. Kim, *J. Mater. Chem. A*, 2016, **4**, 703–750.
19 S. Liu, X. Wang, K. Wang, R. Lv and Y. Xu, *Appl. Surf. Sci.*, 2013, **283**, 732–739.
20 J. Miao, H. B. Yang, S. Y. Khoo and B. Liu, *Nanoscale*, 2013, **5**, 11118–11124.
21 K. S. Ranjith, P. Saravanan, V. T. P. Vinod, J. Filip, M. Cerník and R. T. Rajendra Kumar, *Catal. Today*, 2016, **278**, 271–279.
22 S. Khanchandani, P. K. Srivastava, S. Kumar, S. Ghosh and A. K. Ganguli, *Inorg. Chem.*, 2014, **53**, 8902–8912.
23 A. P. Singh, N. Kodan, B. R. Mehta, A. Held, L. Mayrhofer and M. Moseler, *ACS Catal.*, 2016, **6**, 5311–5318.
24 A. Torabi and V. N. Staroverov, *J. Phys. Chem. Lett.*, 2015, **6**, 2075–2080.
25 M. H. Hsu, C. J. Chang and H. T. Weng, *ACS Sustainable Chem. Eng.*, 2016, **4**, 1381–1391.
26 X. Q. Meng, H. Peng, Y. Q. Gai and J. Li, *J. Phys. Chem. C*, 2010, **114**, 1467–1471.
27 A. Bera and D. Basak, *ACS Appl. Mater. Interfaces*, 2010, **2**, 408–412.
28 S. Jeong, M. Choe, J. W. Kang, M. W. Kim, W. G. Jung, Y. C. Leem, J. Chun, B. J. Kim and S. J. Park, *ACS Appl. Mater. Interfaces*, 2014, **6**, 6170–6176.
29 C. Kirchner, T. Liedl, S. Kudera, T. Pellegrino, A. M. Javier, H. E. Gaub, S. Stolzle, N. Fertig and W. J. Parak, *Nano Lett.*, 2005, **5**, 331–338.
30 A. Sadollahkhani, A. Hatamie, O. Nur, M. Willander, B. Zargar and I. Kazeminezhad, *ACS Appl. Mater. Interfaces*, 2014, **6**, 17694–17701.
31 J. H. Wendorff, S. Agarwal and A. Greiner, *Electrospinning: materials, processing, and applications*, John Wiley & Sons, 2012.
32 S. Tarish, A. A. Haddad, R. Xu, D. Cao, Z. Wang, S. Qu, G. Nabia and Y. Lei, *J. Mater. Chem. C*, 2016, **4**, 1369–1374.
33 T. Yan, H. Liu, P. Gao, M. Sun, Q. Wei, W. Xu, X. Wang and B. Du, *New J. Chem.*, 2015, **39**, 3964–3972.
34 L. Ye, X. Liu, Q. Zhao, H. Xie and L. Zan, *J. Mater. Chem. A*, 2013, **1**, 8978–8983.
35 A. Senthamizhan, B. Balusamy, Z. Aytac and T. Uyar, *CrystEngComm*, 2016, **18**, 6341–6351.
36 J. Rouhi, M. H. Mamat, C. H. R. Ooi, S. Mahmud and M. R. Mahmood, *PLoS One*, 2015, **10**, e0123433.
37 A. B. Korczyc, K. Sobczak, P. Dłużewski, A. Reszka, B. J. Kowalski, Ł. Kłopotowski, D. Elbaum and K. Fronc, *Phys. Chem. Chem. Phys.*, 2015, **17**, 24029–24037.
38 M. A. Osman, A. A. Othman, W. A. El-Said, A. G. A. Elrahim and A. A. Abusehly, *J. Phys. D: Appl. Phys.*, 2016, **49**, 055304.
39 S. Joicy, R. Saravanan, D. Prabhu, N. Ponpandian and P. Thangadurai, *RSC Adv.*, 2014, **4**, 44592–44599.
40 A. Brayek, S. Chaguetmi, M. Ghoul, I. B. Assaker, A. Souissi, L. Mouton, P. Beaunier, S. Nowak, F. Mammeri, R. Chtourou and S. Ammar, *RSC Adv.*, 2016, **6**, 30919.
41 X. Zhang, J. Qin, R. Hao, L. Wang, X. Shen, R. Yu, S. Limpanart, M. Ma and R. Liu, *J. Phys. Chem. C*, 2015, **119**, 20544–20554.
42 J. Wang, Z. Wang, B. Huang, Y. Ma, Y. Liu, X. Qin, X. Zhang and Y. Dai, *ACS Appl. Mater. Interfaces*, 2012, **4**, 4024–4030.
43 Y. Hu, H. Qian, Y. Liu, G. Du, F. Zhang, L. Wang and X. Hu, *CrystEngComm*, 2011, **13**, 3438–3443.
44 J. Schrier, D. O. Demchenko, L. W. Wang and A. P. Alivisatos, *Nano Lett.*, 2007, **7**, 2377–2382.
45 J. Lahiri and M. Batzill, *J. Phys. Chem. C*, 2008, **112**, 4304–4307.
46 Z. Wang, S. W. Cao, S. C. J. Loo and C. Xue, *CrystEngComm*, 2013, **15**, 5688–5693.
47 M. Y. Lu, J. Song, M. P. Lu, C. Y. Lee, L. J. Chen and Z. L. Wang, *ACS Nano*, 2009, **3**, 357–362.

